PAPER

Check for updates

WS₂/g-C₃N₄ composite as an efficient heterojunction photocatalyst for biocatalyzed artificial photosynthesis†

Peng Zeng,[ab] Xiaoyuan Ji,[ac] Zhiguo Su[a] and Songping Zhang [ID] *[a]

A heterogeneous WS₂/g-C₃N₄ composite photocatalyst was prepared by a facile ultrasound-assisted hydrothermal method. The WS₂/g-C₃N₄ composite was used for photocatalytic regeneration of NAD⁺ to NADH, which were coupled with dehydrogenases for sustainable bioconversion of CO₂ to methanol under visible light irradiation. Compared with pristine g-C₃N₄ and the physical mixture of WS₂ and g-C₃N₄, the fabricated WS₂/g-C₃N₄ composite catalyst with 5 wt% of WS₂ showed the highest activity for methanol synthesis. The methanol productivity reached 372.1 μmol h⁻¹ g_cat⁻¹, which is approximately 7.5 times higher than that obtained using pure g-C₃N₄. For further application demonstration, the activity of the WS₂/g-C₃N₄ composite catalyst toward photodegradation of Rhodamine B (RhB) was evaluated. RhB removal ratio approaching 100% was achieved in 1 hour by using the WS₂/g-C₃N₄ composite catalyst with 5 wt% of WS₂, at an apparent degradation rate approximately 2.6 times higher than that of pure g-C₃N₄. Based on detailed investigations on physiochemical properties of the photocatalysts, the significantly enhanced reaction efficiency of the WS₂/g-C₃N₄ composite was considered to be mainly benefiting from the formation of a heterojunction interface between WS₂ and g-C₃N₄. Upon visible-light irradiation, the photo-induced electrons can transfer from the conduction band of g-C₃N₄ to WS₂, thus recombination of electrons and holes was decreased and the photo-harvesting efficiency was enhanced.

1. Introduction

With the increasing concerns regarding the energy crisis and greenhouse gas emissions, it has become urgent to develop a new channel to achieve the conversion of CO_2 to low-carbon fuel.[1–5] Among the energy conversion systems, methanol conversion from CO_2 by a cascade catalyzed by formate dehydrogenase (FateDH), formaldehyde dehydrogenase (FaldDH) and alcohol dehydrogenase (ADH) is considered to be one of the most promising ways.[6,7] However, the regeneration of coenzyme NADH in this multi-enzyme system is the key to the reaction process, since 3 moles of NADH are consumed for every mole of methanol produced.[8,9] In the past decade, inspired by natural photosynthesis, photocatalytic regeneration of coenzyme with the process of reducing CO_2 by multiple enzymes has brought new hope for solving this problem. For the success of such artificial photosynthesis systems, however, the major challenge

is the development of efficient visible-light active photocatalysts.[10–12]

Graphitic carbon nitride (g-C₃N₄), a polymeric semiconductor with a band gap of about 2.7 eV, has attracted significant attention in recent years because of its excellent visible light response,[1,13,14] non-toxicity, low cost, and abundant raw materials. As a visible-light active photocatalyst, g-C₃N₄ has been widely applied for photocatalytic degradation of pollutants, water splitting, and regeneration of NADH since 2009.[15,16] Nevertheless, fast recombination of photogenerated electron–hole pairs and low quantum efficiency limits its further applications. In general, there are three routes to improve the photocatalytic efficiency of g-C₃N₄, which include construction of nanostructure, elemental doping, and hybridization. By fabricating nanosheets,[17] diatom frustule structure,[18] multishell nanocapsules,[19] and some other novel nanostructures,[20] more active sites were exposed on g-C₃N₄ for enhanced light harvesting due to significantly increased specific surface area, and the migration rate of photo-generated electrons was promoted and the recombination of electrons and holes reduced.[18–20] Elemental doping was another widely adopted method for reducing the recombination of electron–hole pairs by replacing the lattice defects of g-C₃N₄.[21,22] Nevertheless, fabrication of new nanostructures and elemental doping often involve complicated preparation process and uncontrollable results. Compared with these above two methods, hybridization of g-

[a]State Key Laboratory of Biochemical Engineering, Institute of Process Engineering, Chinese Academy of Sciences, Beijing 100190, P. R. China. E-mail: spzhang@ipe.ac.cn; Fax: +86 10 82544958; Tel: +86 10 82544958

[b]University of Chinese Academy of Sciences, Beijing, 100049, P. R. China

[c]School of Pharmaceutical Sciences (Shenzhen), Sun Yat-sen University, Guangzhou 510275, P. R. China

† Electronic supplementary information (ESI) available. See DOI: 10.1039/c8ra02807a

C_3N_4 with some other semiconductors was is relative simple but efficient. The hybrid materials, which usually have an unsaturated outer layer electron, can act as a new electron carrier to trap the electrons in the conduction band (CB) of g-C_3N_4 through formation heterojunction or "Z" scheme electron transfer chain.[4,23,24] Nevertheless, either construction of heterojunction or "Z" scheme transfer chain, there are certain requirements for the band structure of hybrid materials, which need a good coordinated relationship with that of g-C_3N_4.

In recent years, transition metal dichalcogenides (TMDCs) have emerged and received tremendous attentions. TMDCs such as WS_2, MoS_2, WSe_2, and $MoSe_2$, have various unique electronic, optical, mechanical and chemical properties, promising their potential applications in electronic devices, transistors, energy storage devices and catalysis.[25–27] Among TMDCs, the 2H-WS_2 has a band gap of about 2.64 V, with conduction band (CB) and valence band (VB) positions at ≈ -1.03 V and 1.61 V versus normal hydrogen electrode,[26,28] respectively; which means the WS_2 possesses energy level of CB and VB both lower than that of g-C_3N_4, but the CB offset between g-C_3N_4 and WS_2 is much shorter than the band gap of g-C_3N_4. Therefore, there would be a perfect band structure coordination between WS_2 and g-C_3N_4 to construct a heterojunction structure. The good match for the energy level would possibly enable fast transfer of the photo-induced electrons in the CB of g-C_3N_4 to the CB of WS_2 before recombination with holes in VB of itself, so that the light harvesting efficiency and utilization of photo-induced electrons would be improved largely.[29–32]

In this present work, a heterogeneous WS_2/g-C_3N_4 composite photocatalyst was prepared via ultrasound assisted hydrothermal method. The photocatalytic performance was evaluated through the regeneration of NADH and degradation of RhB under visible light. Detailed investigations of the physiochemical and photochemical properties of the photocatalysts were performed to elucidate the photoinduced electron-transfer mechanism involved in the heterogeneous WS_2/g-C_3N_4 composite photocatalyst. Therefore, our work highlights the promise of constructing heterojunction based on g-C_3N_4 for photocatalyzed NADH regeneration and pollutant degradation, and encourages further in-depth investigations of this novel type of heterojunction for artificial photocatalysis.

2. Experimental section

2.1. Material

Formate dehydrogenase (FateDH), formaldehyde dehydrogenase (FaldDH), yeast alcohol dehydrogenase (ADH), β-nicotinamide adenine dinucleotide (β-NAD$^+$), reduced nicotinamide adenine dinucleotide (NADH), dicyandiamide, triethanolamine (TEOA), dichloro (pentamethylcyclopentadienyl) rhodium(III) dimer, 1,10-phenanthroline were purchased from Sigma-Aldrich. Tungsten disulfide (WS_2) was purchased from Shanghai Macklin Biochemical Co., Ltd (Shanghai, China).

The organometallic electron mediator (M), [Cp*Rh(phen)H_2O]$^{2+}$, (Cp* = 5-C5Me5, phen = 1,10-phenanthroline) was synthesized as follows. Briefly, 103.01 mg of dichloro

(pentamethylcyclopentadienyl) rhodium(III) dimer was added to 10 mL of methylene chloride, where the solid was insoluble. Then, 60.07 mg of 1,10-phenanthroline was added to the mixture. After stirring at room temperature for 3 h, the color of the solution changed from dark orange to orange. After removing the solvent by evaporation under reduced pressure, M was obtained.

2.2. Preparation of g-C_3N_4 and WS_2/g-C_3N_4 composites catalysts

To prepare graphite phase carbon nitride (g-C_3N_4), 10 g of dicyandiamide was ground into a powder and placed in a capped alumina crucible covered with aluminum foil and then calcined at 550 °C for 4 hours in a muffle furnace at a rate of 3 °C min^{-1}. The g-C_3N_4 was obtained as yellow solid.

WS_2/g-C_3N_4 composites were synthesized via a two-step self-assembly procedure. Herein, 100 mg of g-C_3N_4 was added into 100 mL deionized water and sonicated for one hour. Into the above suspension, definite amount of WS_2 powder was added to obtain a WS_2 mass fraction of 1, 5, 10%. The suspension mixture was sonicated for 30 min followed by 36 h mechanical stirring. To consolidate the heterojunction interface in the WS_2/g-C_3N_4 composites, the mixture was sealed into a 100 mL Teflon-lined stainless steel autoclave and heated to 140 °C for 6 h. After cooling down to room temperature and evaporating the solvent, WS_2/g-C_3N_4 composites with different composition proportions were obtained.

2.3. Catalyst characterization

Scanning electron microscope (SEM) analysis was performed on a JSM 6700F cold field emission scanning electron microscope at beam energy of 10.0 kV. Transmission electron microscope (TEM) images were taken on JEM 2100F instrument at an acceleration voltage of 200 kV. Atomic force microscopy was performed using Bruker FASTSCANIO microscope. Thermo gravimetric analysis (TGA), was carried out in a flow of nitrogen gas (10 mL min^{-1}) at a heating rate of 10 °C min^{-1} using Synchronous DSC-TGA Thermal Analysis (SDT Q600). The specific surface areas were measured on ASAP 2020HD88 by the BET method. The crystal structures of WS_2/g-C_3N_4 composites were identified by X-ray diffraction (XRD) with Empyrean X-ray diffractometer from PANalytical B.V. of the Netherlands. X-ray photoelectron spectroscopy (XPS) analysis was performed on ESCALAB 250Xi instrument. The Fourier transform infrared (FT-IR) spectra were collected from 400 to 4000 cm^{-1} at the spectral resolution of 0.482 cm^{-1} on NICOLET iS 50 infrared spectrometer. UV-vis diffuse reflectance spectroscopy (UV-vis DRS) were recorded in the range of 200–900 nm by a TU-1901 spectrophotometer with the reference of $BaSO_4$. Photoluminescence (PL) spectra were determined on a NanoLOG-TCSPC steady state/transient fluorescence spectrometer. The wavelength of the excitation light was 340 nm.

2.4. Photocatalytic regeneration of NADH

The photocatalytic regeneration of NADH reaction was carried out in a side-irradiation vial under an irradiation of 300 W Xe

lamp with a 400 nm cut-off filter. In the regeneration procedure, the reaction medium (3 mL) was composed of NAD^+ (1 mM), TEOA (15 w/v%), M (0.25 mM), phosphate buffer (100 mM, pH 7.0) and catalyst (3 mg). The distance between reactor and Xe lamp was fixed at 20 cm. Before irradiation, the reaction solution was placed in a dark environment for 1 h to achieve adsorption–desorption equilibrium. The concentration of NADH regenerated from NAD^+ was monitored by measuring the absorbance at 340 nm ($\varepsilon^{NADH} = 6.22$ mM^{-1} cm^{-1}) using a UV-vis spectrophotometer (UV-2800, Unico).

2.5.   Conversion CO_2 to methanol

The conversion of CO_2 to methanol was performed in quartz reactor. The reaction solution was composed of 3 mg catalyst, NADH (1 mM), $KHCO_3$ (0.1 M), 15 w/v% triethanolamine (TEOA), M (0.125 mM), FateDH (0.2 mg), FaldDH (0.3 mg), and ADH (1.5 mg) in 2 mL 0.1 M PBS buffer (pH 7.0). Prior to the addition of enzyme, the PBS buffer was firstly saturated with gaseous CO_2. The amount of methanol was detected by gas chromatograph as described in our previous reports.[11]

2.6.   Degradation of RhB

The degradation of RhB was performed in quartz reactor. The photocatalytic reaction system consisted of 300 W Xe lamp with a 400 nm cut-off filter. All experiments were conducted at room temperature. In a typical run, 5 mg of catalysts was added into 5 mL of 10 mg L^{-1} RhB solution. Prior to irradiation, the suspension was magnetically stirred in the dark for 1 h to ensure the adsorption–desorption equilibrium. The concentration of RhB was monitored by measuring the absorbance at 554 nm using a UV-vis spectrophotometer (UV-2800, Unico). The procedures of the scavenging experiments of reactive oxygen species were similar to that of the photo degradation experiment. Various scavengers, including isopropyl alcohol (IPA, 1 mM), TEOA (1 mM), KI (1 mM), and 0.5 h nitrogen purging (N_2) were subjected into the RhB solution prior to irradiation.

3.   Results and discussions

3.1.   Fabrication and characterization of $WS_2/g-C_3N_4$ composites

The $WS_2/g-C_3N_4$ composites were fabricated by a two-step self-assembly procedure, the morphologies of $g-C_3N_4$, WS_2 and the 5 wt% $WS_2/g-C_3N_4$ composites were observed by TEM. As shown in Fig. 1a, a stacked layer structure is clearly observed in the $g-C_3N_4$ sample, which is consistent with existing reports.[33] The WS_2 sample displays a structure of hexagonal lamellar stacking (Fig. 1b).[34] For $WS_2/g-C_3N_4$ composites, $g-C_3N_4$ is found to be covered by WS_2. The darker part with hexagonal shape in Fig. 1c
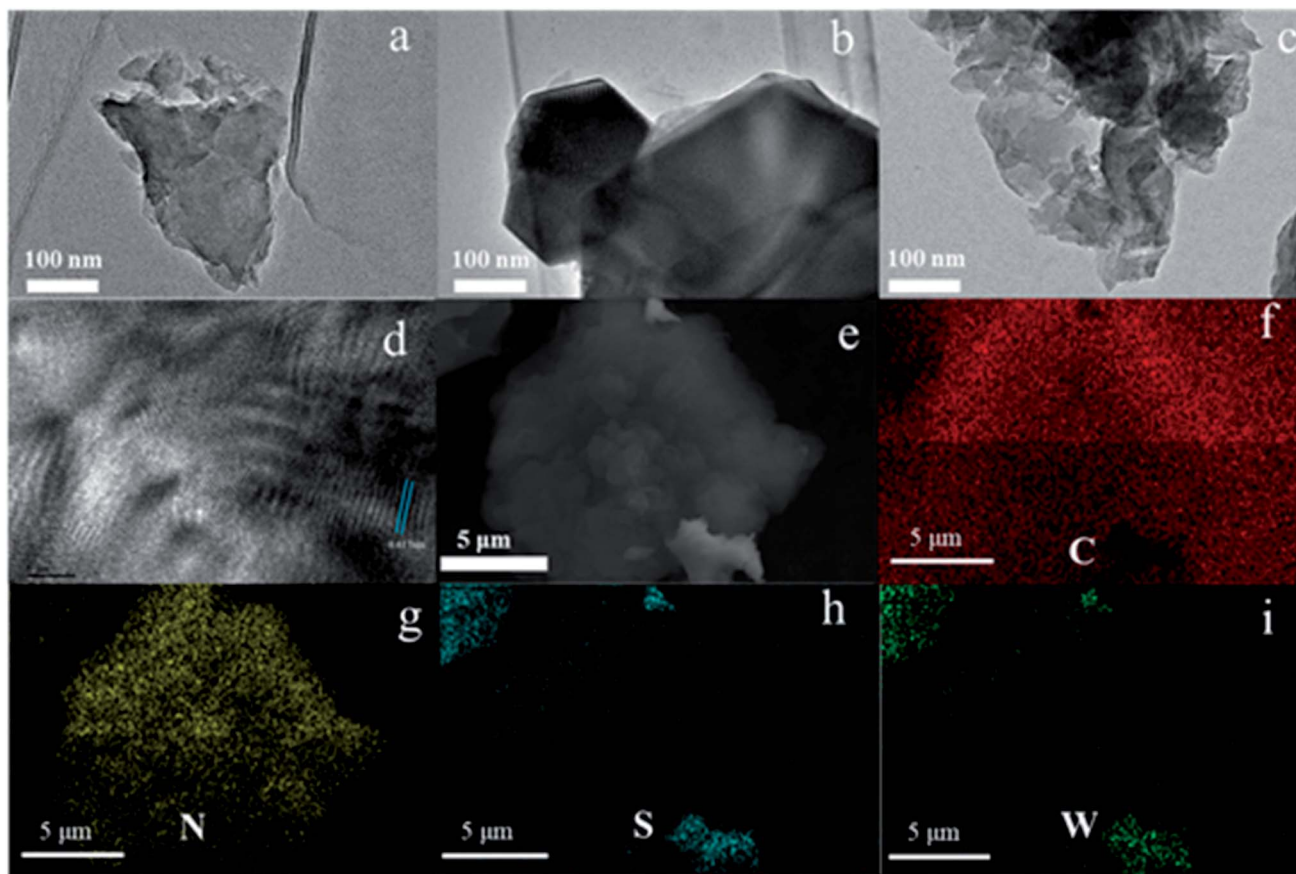

Fig. 1   TEM images of (a) $g-C_3N_4$, (b) WS_2, (c) 5 wt% $WS_2/g-C_3N_4$ composite and its (d) HRTEM image. (e–i) SEM and the corresponding elemental mapping of C, N, S, and W elements in 5 wt% $WS_2/g-C_3N_4$ composite.

should be WS_2 and the lighter part is g-C_3N_4, which demonstrates the well distribution of WS_2 on g-C_3N_4. The high-resolution TEM image shows the microstructure of the WS_2/g-C_3N_4 composite, in which the interplanar spacing is very close to the 001 plane of WS_2 (Fig. 1d). SEM images (Fig. 1e) of the 5 wt% WS_2/g-C_3N_4 composite and the corresponding energy-dispersive X-ray spectroscopy (EDS) elemental mapping of C, N, S and W, which are characteristic elements of g-C_3N_4 and WS_2, respectively, clearly confirmed the uniform coupling of g-C_3N_4 with WS_2 (Fig. 1f–i). This coupling would be favorable for the charge transfer between WS_2 and g-C_3N_4 and then promotes the separation of photo-generated electron–hole pairs. Moreover, the TGA measurement shows that the decomposition temperature of WS_2/g-C_3N_4 composites is lower than the pristine g-C_3N_4. Similar phenomena were also observed in some other g-C_3N_4-based heterojunction, such as g-C_3N_4/AgBr/Fe_3O_4, SnO_{2-x}/g-C_3N_4, TiO_2/g-C_3N_4, $DyVO_4$/g-C_3N_4, g-C_3N_4/$SmVO_4$.[24,35–37] The shift of weight loss towards lower temperature was considered due to some changes in surface chemistry of the g-C_3N_4 during forming of heterojunction structure with other materials (Fig. 2).[38,39]

XRD were adopted to analyze the composition and structure of as-prepared WS_2/g-C_3N_4 composites. To understand the crystallization of the composite and also mutual interface of

each semiconductor over the other during composite formation, the XRD patterns of the following materials were presented in Fig. 3a, which include the obtained WS_2, hydrothermally treated WS_2 (referred as HT WS_2) and ultrasonicated WS_2 (referred as US WS_2) in absence of g-C_3N_4; as formed g-C_3N_4; ultrasonicated 5% WS_2/g-C_3N_4 composite (US 5% WS_2/g-C_3N_4), hydrothermally treated (HT 5% WS_2/g-C_3N_4), as well as the 5% WS_2/g-C_3N_4 composites fabricated through combined ultrasonication-hydrothermal treatments. As shown in Fig. 3a, the XRD pattern of obtained g-C_3N_4 showed the typical diffraction peaks at 13.1° and 27.3°, perfectly indexed as the (100) and (002) planes, respectively, which were ascribed to in-planar tri-s-triazine unit and the interplanar stacking of aromatic systems.[17,40–44] The XRD patterns of the obtained WS_2 exhibit many distinct diffraction peaks, indicating its hexagonal structure,[28,34] which is consistent with the 2H configuration in the standard card library. The HT WS_2 and US WS_2 presents the same XRD as that of the obtained WS_2, indicating the crystallization of WS_2 was not affected by ultrasonication and hydrothermal treatments. For the 5% WS_2/g-C_3N_4 composites, the XRD patterns of all the three composites display the combination of the two sets of diffraction data for both g-C_3N_4 and WS_2 and no other phase is detected, implying that WS_2 was not incorporated into the lattice of g-C_3N_4.

The FT-IR was also adopted to test the obtained g-C_3N_4, WS_2, and WS_2/g-C_3N_4 composite. As shown in Fig. 3b, pure g-C_3N_4 has a much stronger IR response than WS_2, and the addition of WS_2 shows no obvious effect on the IR spectrum of g-C_3N_4. For the g-C_3N_4, the strong bands in the region of 1200–1700 cm^{-1} are assigned to the typical stretching vibration modes of C–N heterocycles. The peaks at 3000–3700 cm^{-1} represent the N–H and O–H stretching vibration. The sharp peak at 810 cm^{-1} originates from the characteristic breathing mode of tri-s-triazine units.[45–49] For the WS_2/g-C_3N_4 composites, the overall patterns of the spectra are the same as the g-C_3N_4, confirming the existence of heptazine heterocyclic rings in WS_2/g-C_3N_4 composites. In generally, there is no obvious difference from the FTIR spectrogram before and after doping, but it's not difficult for us to see that the position of the characteristic peak from the tri-s-triazine vibration of g-C_3N_4 has a certain degree of shift (Fig. 3c), indicating that there might be some interactions
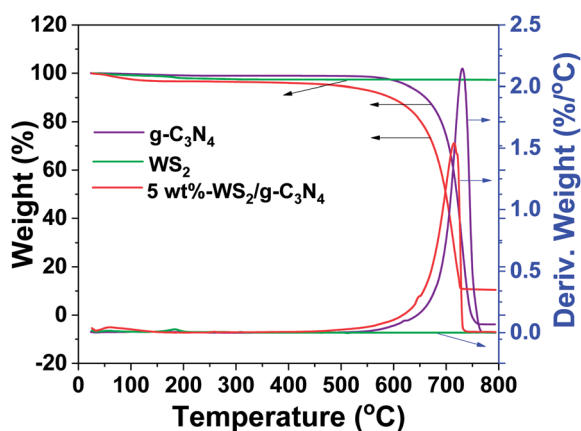

Fig. 2 TGA profiles of g-C_3N_4, WS_2 and 5 wt% WS_2/g-C_3N_4 composite.
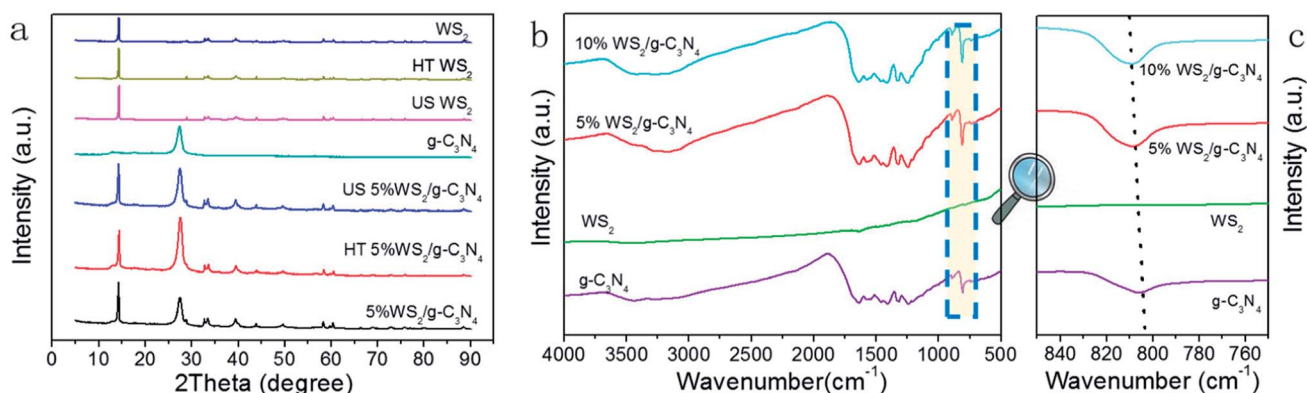

Fig. 3 (a) XRD patterns and (b) FT-IR spectra of obtained g-C_3N_4, WS_2, WS_2/g-C_3N_4 composites; (c) local magnification of the FT-IR spectra at around 810 cm^{-1} of spectra in (b).

between the "nitrogen pots" of g-C_3N_4 and W species of WS_2.[24] As a complement to FT-IR, the Raman spectra of the g-C_3N_4 and the 5% WS_2/g-C_3N_4 were also recorded. As shown in Fig. S1,† the catalysts show several very weak distinctive peaks at 458, 679 and 1220 cm^{-1}, which is basically consistent with the situation of g-C_3N_4 reported in the literatures.[50,51] The formation of 5% WS_2/g-C_3N_4 composite did not lead to apparent new peak, which may be due to the strong photoluminescence effect of g-C_3N_4 and the small faction of WS_2 in the composite.

X-ray photoelectron spectroscopy (XPS) analysis was employed to determine the chemical composition and bonding configuration of the g-C_3N_4, WS_2 and the WS_2/g-C_3N_4 composites (Fig. 4a), with the high-resolution spectrum of each sample were illustrated in Fig. 4b–d. The survey XPS spectra shown in Fig. 4a indicate that the prepared WS_2/g-C_3N_4 samples are composed of C, N, W and S. Specifically, the C1s spectrum (Fig. 4d1) of WS_2/g-C_3N_4 composites show there are two C1s peaks located at 284.7 and 288.2 eV, the former is ascribed to the adventitious hydrocarbon from the XPS instrument, while the latter is assigned to sp^2-bonded carbon atom (N–C=N) of g-C_3N_4 in aromatic rings. The high-resolution N1s spectrum of the WS_2/g-C_3N_4 composites could be fitted into four peaks (Fig. 4d2). The peaks centered at 398.7 and 399.5 eV were attributed to sp^2-hybridized nitrogen atom (C=N–C group) and tertiary nitrogen (N–C$_3$ group or H–N–C$_2$), respectively; the peaks at 401.0 and 404.7 eV derived from amino function groups and charging effect localization in heterocycles, respectively.[4,24,52] As compared with the C1s and N1s spectrum (Fig. 4b1 and b2) of pure g-C_3N_4, all
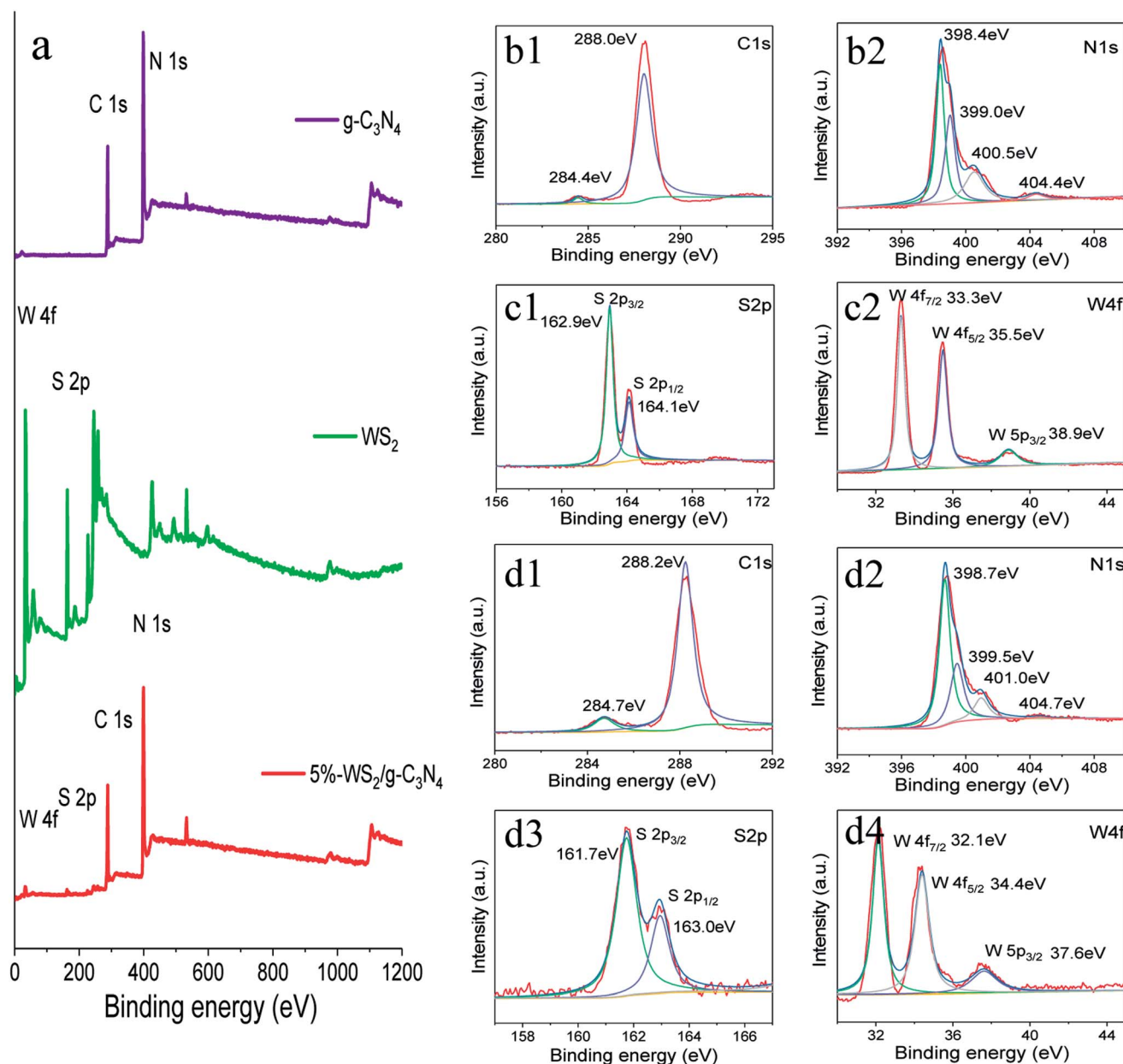

Fig. 4 The XPS survey spectra of (a) g-C_3N_4, WS_2 and 5 wt% WS_2/g-C_3N_4 composite. High resolution C1s (b1), N1s (b2) spectra from g-C_3N_4 and S2p (c1) W4f (c2) spectra from WS_2, as well as C1s (d1), N1s (d2), S2p (d3), W4f (d4) spectra from 5 wt% WS_2/g-C_3N_4 composite.

those peaks of the WS_2/g-C_3N_4 composites shifted to a position with a higher binding energy.

Fig. 4d3 and d4 display the S2p spectra and the W4f spectra of the WS_2/g-C_3N_4 composites. The peaks at 161.7 and 163 eV can be ascribed to the S^{2-} species, donated as $S2p_{3/2}$ and $S2p_{1/2}$, respectively;[34] the W4f peaks at 32.1, 34.4, and 37.6 eV can be ascribed to the W^{4+} species, donated as $W4f_{7/2}$, $W4f_{5/2}$ and $W5p_{3/2}$.[28,53] In contrast to the W4f and S2p spectrum (Fig. 4c1 and c2) of WS_2, all these above peaks of the WS_2 shifted to a position with a lower binding energy after coupling with g-C_3N_4. Thus, the C1s and N1s peaks of g-C_3N_4 shifted toward the higher binding energy, while the W4f and S2p peaks of WS_2 shifts towards the lower binding energy. It was suggested that there might be some S–C chemical bonds formed between the heterojunction interfaces of WS_2/g-C_3N_4 composites, thus electron transfer could occur from g-C_3N_4 to WS_2 at this interfaces due to their different electron concentration.[24,54]

The optical properties of WS_2, g-C_3N_4 and the WS_2/g-C_3N_4 composites were revealed by the UV-vis diffuse reflectance spectra (DRS). As shown in Fig. 5a, pure g-C_3N_4 had absorption from UV to visible region, with an absorption edge at 460 nm, which corresponding to a band gap about 2.7 eV according to the Kubelka–Munk conversion (Fig. 5b).[55,56] However, with the coupling of WS_2, the absorption range of the composite became wider than that of pure g-C_3N_4, a remarkable enhanced light-harvesting ability is observed for the WS_2/g-C_3N_4, and the band gap width estimated from the K–M equation became narrower accordingly, which implied that the light absorption ability of the WS_2/g-C_3N_4 composites became stronger. The coupling of WS_2 on g-C_3N_4 may generate an impurity energy level in the valence band (VB) and narrow the band gap. The defect energy levels increased the light absorption efficiency of the materials and thus may exhibit photocatalytic performance superior to that of the individual material. In addition, the DRS spectra of US 5% WS_2/g-C_3N_4 and HT 5% WS_2/g-C_3N_4 composites were also measured and compared with that of the 5% WS_2/g-C_3N_4, it is indicated that the omitting the ultrasonication or hydrothermal treatments during composite formation lead to negligible changes in the band structure (Fig. S2†).

Fig. 6 presents the BET surface areas measurement of 5 wt% WS_2/g-C_3N_4 composites. For comparison, the surface areas of g-C_3N_4 and the physical mixture of g-C_3N_4 with 5 wt% WS_2 (referred as PM-WS_2/g-C_3N_4 in the following text) were also determined, the results were listed in Table S2.† The specific surface area of g-C_3N_4 was 7.34 m^2 g^{-1}, which is similar to the value reported by He et al.,[24] but lower than those reported for most g-C_3N_4 nanosheets,[54,57] which indicates that the g-C_3N_4 has multi-layered structure. Slight decrease in surface area was observed for the PM-WS_2/g-C_3N_4 (6.87 m^2 g^{-1}); while the 5 wt% WS_2/g-C_3N_4 composites exhibited much higher BET values (12.22 m^2 g^{-1}), which indicated that some reactions might have occurred between g-C_3N_4 and WS_2 during recombination. This larger specific surface area of WS_2/g-C_3N_4 composites also could supply more reactive sites for light and substrates, improve the whole efficiency of the reaction. It should be noted that the specific surface area of the 5 wt% WS_2/g-C_3N_4 composites are still far lower than the g-C_3N_4 nanosheets, indicating the ultrasonication and hydrothermal treatments during composite formation still could not result in effective exfoliation of the g-C_3N_4. After BJH (Barrett–Joyner–Halenda) plotting, the pore size distribution of each samples were analyzed (Fig. 6b). Compared with the pure g-C_3N_4, coupling of WS_2 lead to slight decrease in pore diameter.

3.2. Photocatalytic performance for NADH regeneration and CO_2 reduction

Conversion of CO_2 to methanol through redox multienzymatic cascade reaction has been widely explored.[7,10,12] However, consumption of the expensive NADH cofactor at stoichiometric ratios imposes great hurdles to the practice of these processes. Here in the present work, we intended to develop a biocatalyzed artificial photosynthesis system by coupling the reduction of CO_2 catalyzed by FateDH, FaldDH, and ADH with the newly developed WS_2/g-C_3N_4 composite as the photocatalyst to regenerate NADH using solar energy.

Based on the above photochemical investigations of the g-C_3N_4 and the WS_2/g-C_3N_4 composites, their performance for visible light-driven photocatalytic NADH regeneration were
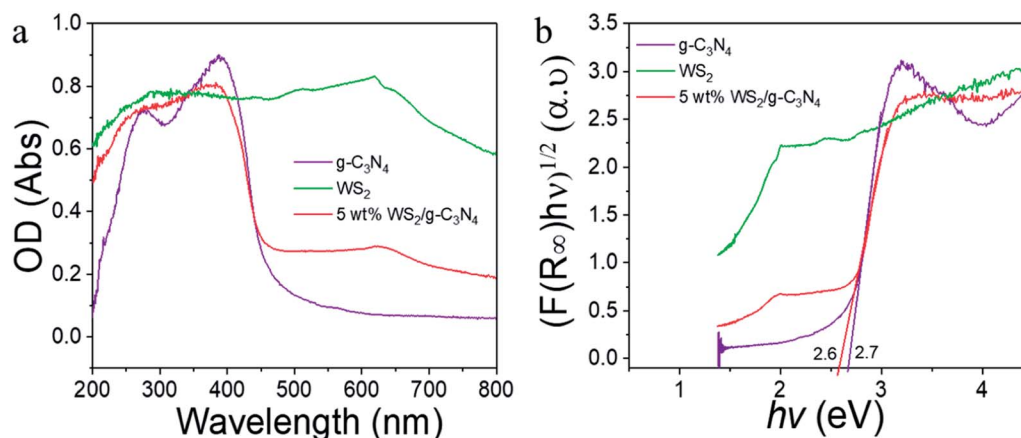

Fig. 5 (a) UV-vis diffuse reflection spectra of pure g-C_3N_4, WS_2 and 5 wt% WS_2/g-C_3N_4 composite; (b) corresponding bandgap of pure g-C_3N_4, WS_2 and 5 wt% WS_2/g-C_3N_4 composite estimated from Kubelka–Munk equation.
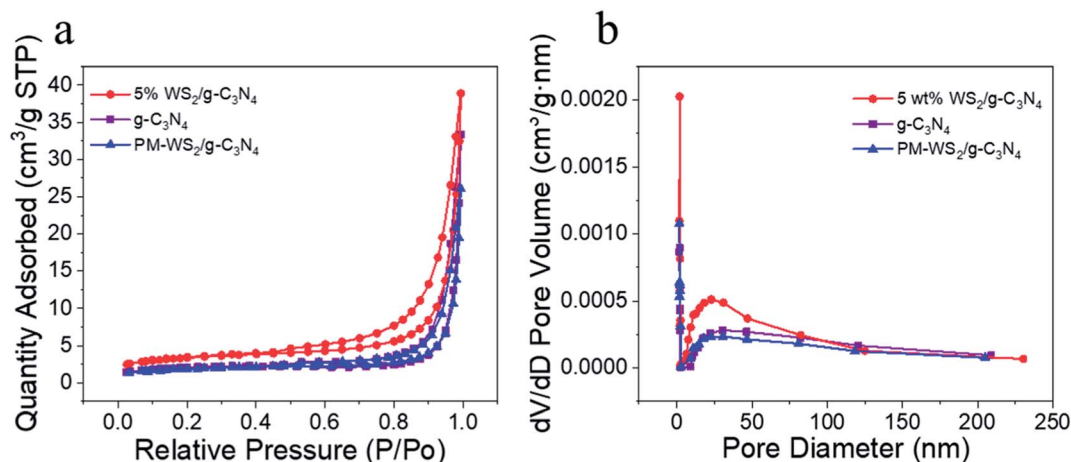
Fig. 6 (a) The N_2 adsorption/desorption isotherms, (b) the corresponding pore-size distribution. BET surface area was measured by nitrogen sorption isotherms at 77.5 K and up to 1.03 bar.

examined. The reactant solution consisted of 15 wt% TEOA, 0.25 mM electron mediator M, and NAD^+ with an initial concentration of 1 mM and an active $g-C_3N_4$ content of 1 mg mL^{-1} was maintained in all the experiments. The photocatalytic activity comparison among pure $g-C_3N_4$, WS_2, PM-WS_2/$g-C_3N_4$ and WS_2/$g-C_3N_4$ composite with WS_2 content of 1%, 5% and 10% are presented in Fig. 7a. The monolithic $g-C_3N_4$ and WS_2 had rather low catalytic efficiency, NADH regeneration yield at 6 h was below 10%. By physically mixing 5 wt% WS_2 with $g-C_3N_4$, the NADH photo-regeneration yield enhanced to 15%. While the 5 wt% WS_2/$g-C_3N_4$ composite presents the best performance, a NADH yield of 37.1% was achieved, which were about four times of those obtained by using monolithic $g-C_3N_4$ and WS_2. With further increasing the WS_2 content in the composite to 10 wt%, however, leading to decrement in activity for the photo-regeneration of NADH. Presumably, coupling of high amount WS_2 may lead to shielding of active site of $g-C_3N_4$ by WS_2 or loss of favorable interfaces between $g-C_3N_4$ and WS_2. Similar phenomenon was also observed on the activity of

mesoporous graphitic carbon nitride (mpg-CN) loaded with WS_2 towards H_2 generation. About 0.3 at% WS_2 loading amount was found optimal to reach highest rate of hydrogen evolution, and heavy loading of WS_2 led to decrease in activity of the heterojunctions photocatalyst.[29]

To justify the necessity of multiplicative steps involving ultrasonication, mechanical stirring and hydrothermal treatment for the preparation of WS_2/$g-C_3N_4$, a series of WS_2/$g-C_3N_4$ composites were prepared by simpler steps and evaluated for its activity towards NADH photoregeneration. Results presented in Fig. S3 and Table S3† clearly indicated that either omitting of the ultrasonication or hydrothermal treatments, or even the mechanical stirring between these two operations during composite formation, led to significantly lower activity of the fabricated WS_2/$g-C_3N_4$. The hydrothermal time and temperature did not show remarkable influence on the activity of the composite photocatalyst. Therefore, the two-step sonication and subsequent hydrothermal treatments are necessary, though somewhat tedious, to ensure the photocatalyst a high activity of
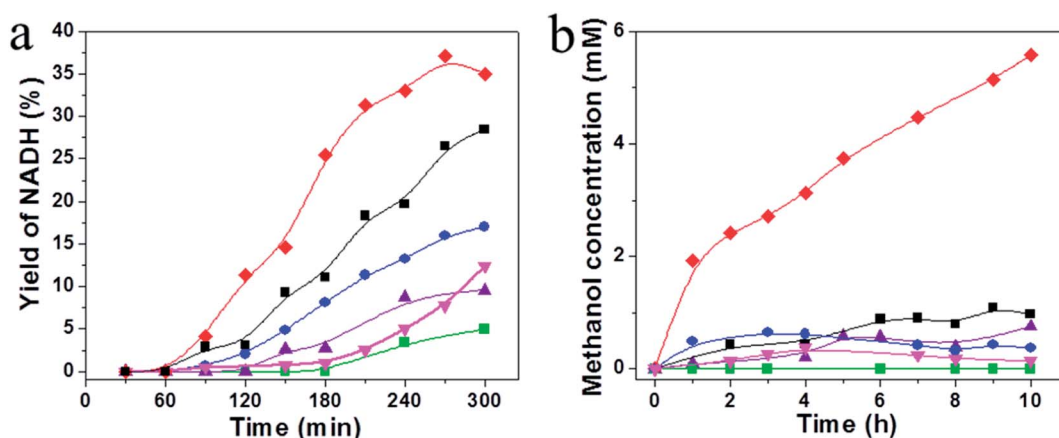

Fig. 7 (a) Photocatalytic NADH regeneration by (▲) $g-C_3N_4$, (■) WS_2, (●) PM-WS_2/$g-C_3N_4$, (▼) 1 wt% WS_2/$g-C_3N_4$, (◆) 5 wt% WS_2/$g-C_3N_4$, and (■) 10 wt% WS_2/$g-C_3N_4$ composite. A reaction medium was composed of photocatalyst (1 mg mL^{-1}), NAD^+ (1 mM), TEOA (15 w/v%) and M (0.25 mM) in 100 mM, pH 7.0 phosphate buffer. (b) The production of methanol as a function of time.

the 5 wt% WS_2/g-C_3N_4 composite, which presents the highest NADH photo regeneration yield of 37.1%. It was believed that the first step of sonication was to ensure a good dispersion of g-C_3N_4 particles, the second step of sonication of g-C_3N_4 and WS_2 mixture was for a full contact between these two materials, which was crucial for the subsequent hydrothermal reaction.

In another set of experiment, we tried to address the more challenging question of a potential mediator-free regeneration of NADH. To our surprise, the mediator-free with system with 5 wt% WS_2/g-C_3N_4 composite as photocatalyst was also possible, though the regeneration yield at 6 h was only about half of that obtained in presence of M (Fig. S3, Table S3†). This can be explained from the following two points. Firstly, a mixture of 1,4-NADH and 1,6-NADH would possibly formed, while in presence of M, 1,4-NADH will be unique production; secondly, without a strong redox agent, *i.e.*, mediator, g-C_3N_4 also catalyzes the back reaction, meaning an equilibrium between NAD^+ and NADH.[18]

We then evaluated the WS_2/g-C_3N_4 composite as a photocatalyst of the artificial photosynthesis system for bioconversion of CO_2 to methanol. As expected, the photocatalysts showed higher activity for NADH regeneration also exhibited

higher efficiency for methanol synthesis from CO_2, when the NADH photoregeneration process was coupled with the biocatalytic process. The highest methanol concentration up to 5.58 mM were obtained by using 5 wt% WS_2/g-C_3N_4 composite as photocatalysts, corresponding to a methanol productivity of 372.1 μmol h^{-1} g_{cat}^{-1}, which was about 7.5 times higher than that obtained by using g-C_3N_4 (50.31 μmol h^{-1} g_{cat}^{-1}). This result clearly indicated that the formation of WS_2/g-C_3N_4 heterojunction generated significant photo-synergistic effect and played key roles in the enhancement in the photocatalytic activity.

3.3. Photocatalytic performance for RhB degradation

To further demonstrate the effectiveness of formation of heterojunction structures between the components of the WS_2/g-C_3N_4 composites, the photocatalytic activity of the composites for the degradation of RhB was also evaluated, and results were compared with pure g-C_3N_4 and WS_2. As shown in Fig. 8a, the degradation ratio of RhB reached to about 100% by using the 5 wt% WS_2/g-C_3N_4 composites under visible light irradiation for 60 min, which was much higher than the corresponding
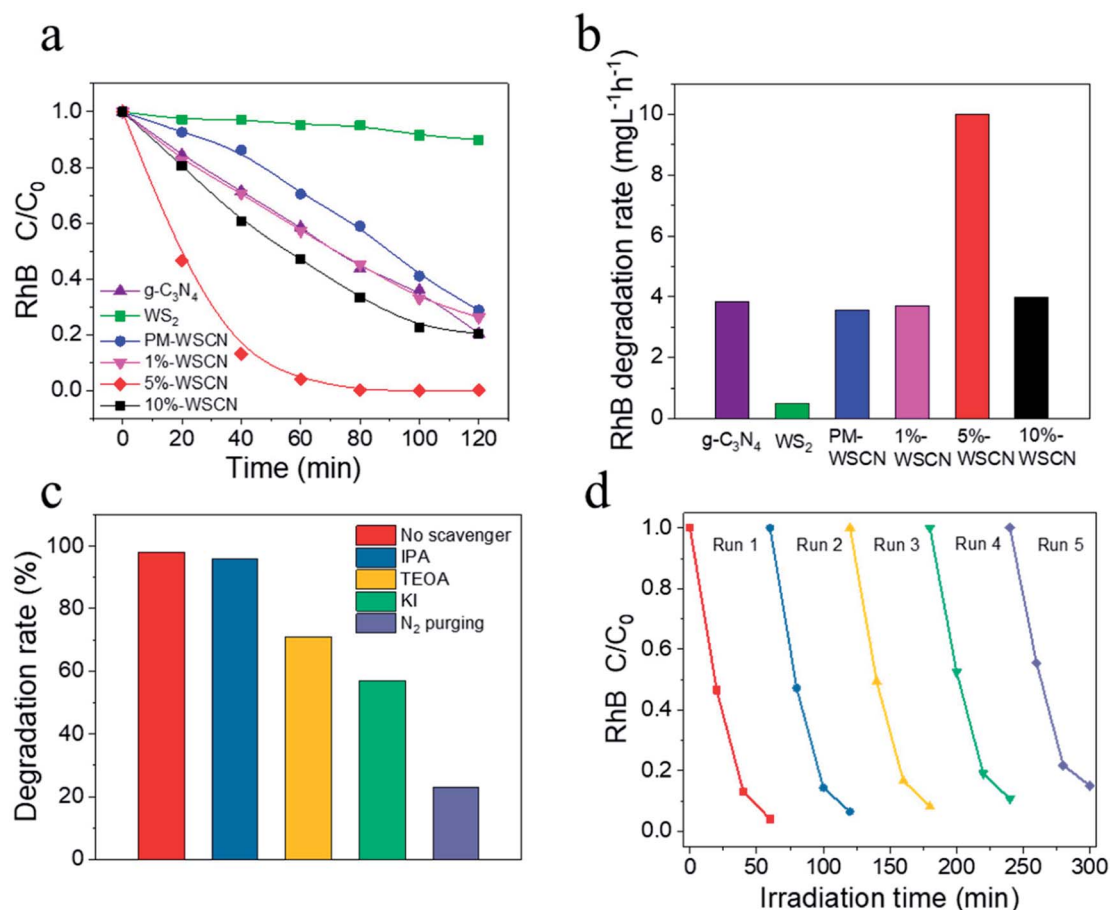

Fig. 8 (a) Photocatalytic degradation profiles of RhB under visible light irradiation in the presence of (▲) g-C_3N_4, (■) WS_2, (●) PM-WS_2/g-C_3N_4, (▼) 1 wt% WS_2/g-C_3N_4, (♦) 5 wt% WS_2/g-C_3N_4, and (■) 10 wt% WS_2/g-C_3N_4 composite; (b) the comparison chart of RhB degradation rate after 1 h's irradiation catalyzed by various catalysts; (c) effects of different scavengers on degradation of RhB in the presence of 5 wt% WS_2/g-C_3N_4 composite catalyst under visible-light irradiation; and (d) reusability of the 5 wt% WS_2/g-C_3N_4 composite catalyst for five successive runs (each run was lasted for 60 min).
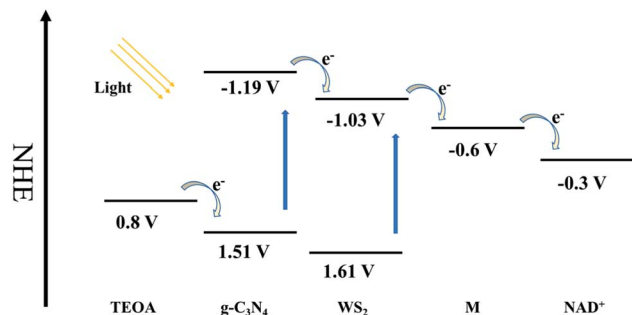
Fig. 9 Schematic diagram of electron flow and energy level during coenzyme regeneration.

degradation ratios obtained by using pristine g-C₃N₄ (~70% at 120 min) and WS₂ (~10% at 120 min), as well as the PM-WS₂/g-C₃N₄ (~70% at 120 min). Fig. 8b presents the apparent degradation rate derived by simple linearly plotting of RhB concentration decrease against irradiation time. The results indicate that the degradation rate using composite photocatalyst containing 5 wt% WS₂ was about 2.6 and 19.7 times higher than that of g-C₃N₄ and WS₂, respectively.

In general, some reactive oxygen species including hydroxyl radicals ($^\bullet$OH) and superoxide radicals ($^\bullet$O$_2^-$), as well as holes (h⁺) are expected to be involved in the photocatalytic process of RhB degradation.[55,58] To investigate the role of these reactive species, the effects of some radical scavengers and N₂ purging on the photodegradation of RhB were studied to propose the possible photocatalytic mechanism. Results in Fig. 8c indicate that the addition of IPA ($^\bullet$OH scavengers) had almost no effect on RhB degradation. While addition of TEOA (h⁺ scavengers) and KI (scavenger of both $^\bullet$OH and h⁺) led the degradation rate after 1 h's irradiation decreased to about 70% and 58%, respectively. When N₂ purging was conducted which acts as $^\bullet$O$_2^-$ scavenger, the degradation rate decreased dramatically to about only 22%. These results suggested that the $^\bullet$O$_2^-$ plays major roles in the photodegradation of RhB catalyzed by the WS₂/g-C₃N₄ heterojunction photocatalyst, which is consistent with results in other reports.[55,58]

Reusability of photocatalyst is a very important parameter from an economical viewpoint. The reusability and stability of

the 5 wt% WS₂/g-C₃N₄ composites was examined by measuring the RhB degradation during repeated usages. As shown in Fig. 8d, after five successive runs, there is no remarkable decrease in its activity. Hence, the photocatalyst has a good stability during the photocatalytic reactions.

3.4. Proposed mechanism

High efficient charge separation was the crucial fact for the improvement of photocatalytic activity. Construction of heterojunction structure is one of the most effective means to improve photocatalytic activity *via* fast and efficient transfer photo-excited electron in the CBs in the heterojunction. In this study, WS₂ was hybridized with g-C₃N₄ to generate an efficient heterojunction structure. Based on the energy band structure of g-C₃N₄ and WS₂, as shown in Fig. 9, the CB and VB of g-C₃N₄ are all higher than that of WS₂.[24,28] Because of the unstable state of photo-generated electrons and holes, they will tend to recombine quickly to achieve steady state. However, due to the distance between CB of g-C₃N₄ and CB of WS₂ is much shorter than the band gap of g-C₃N₄, the CB offset of 0.16 eV will possibly drive the photo-excited electrons on the CB of g-C₃N₄ transfer to the CB of WS₂ before recombination with holes in the VB of g-C₃N₄. Based on the similar mechanism, the holes in the VB of WS₂ tend to transfer to the VB of g-C₃N₄, driven by the VB offset of 0.10 eV. Therefore, an orientated transfer of the charge carrier across the heterojunction interface was realized.

To further demonstrate the photoinduced electron-transfer mechanism, as well as elucidate the effect of amount of WS₂ in WS₂/g-C₃N₄ heterojunction on the overall reaction efficiency, detailed investigations of the photochemical properties were performed on WS₂/g-C₃N₄ heterojunction hybridized with different amount of WS₂ ranging from 1 wt% to 10 wt%. For most semiconductors, photogenerated electrons and holes can bind after the excitation by incident light, leading to the transfer of partial energy to fluorescence. In general, the binding efficiency and photoelectron lifetime can be measured by monitoring fluorescence intensity and lifetime.[17,57,59,60] Fig. 10a presents the fluorescence spectrum of pure g-C₃N₄, which shows strong fluorescence intensity at 437 nm. However, the
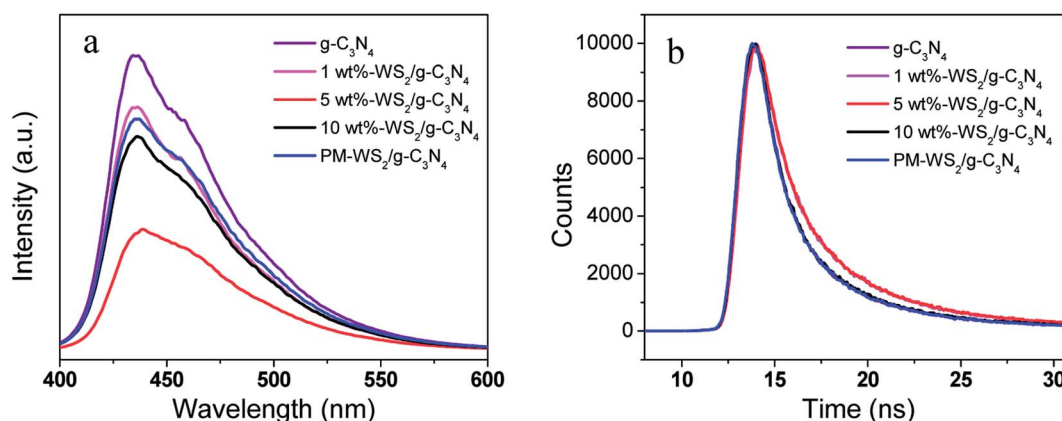

Fig. 10 (a) PL spectra of g-C₃N₄, WS₂ and WS₂/g-C₃N₄ composite photocatalysts. (b) Excited state electron radioactive decay of g-C₃N₄, WS₂ and WS₂/g-C₃N₄ composite.

physical mixing WS_2 and g-C_3N_4 (PM-WS_2/g-C_3N_4) and the WS_2/g-C_3N_4 heterojunction all show a decremental effect on the fluorescence spectra. More interesting, the WS_2/g-C_3N_4 heterojunction with 5 wt% WS_2 presents the lowest fluorescence intensity, which means more electrons on the CB of g-C_3N_4 transfer to WS_2 instead of recombining with the holes in the VB of g-C_3N_4. The suppressed recombination of electron–hole pairs of g-C_3N_4 may attribute to the fast electron transfer from CB of g-C_3N_4 to the CB of WS_2, which also demonstrate the electron transfer mechanism and explain the highest activity of 5 wt% WS_2/g-C_3N_4 heterojunction.

In order to confirm the suppressed recombination of electron–hole pairs in 5 wt% WS_2/g-C_3N_4 heterojunction, time-resolved fluorescence decay analysis was carried out. The excited state electron radioactive decay lifetime (Fig. 10b) show that the 5 wt% WS_2/g-C_3N_4 heterojunction owns the longest fluorescence lifetime (11.080 ns) compared with that of 10 wt% WS_2/g-C_3N_4 (10.549 ns), 1 wt% WS_2/g-C_3N_4 (10.368 ns), PM-WS_2/g-C_3N_4 (10.554 ns), and g-C_3N_4 (10.487 ns), indicating that the incorporation of WS_2 increased the photoelectron lifetime of WS_2/g-C_3N_4. This result further certified that 5 wt% WS_2/g-C_3N_4 heterojunction has the best coordination between g-C_3N_4 and WS_2 for the most efficient and fastest photo-excited electrons transfer.

4.   Conclusions

In summary, we successfully fabricated and applied a heterogeneous WS_2/g-C_3N_4 composite photocatalyst for methanol conversion from CO_2 and pollutant degradation under irradiation of visible light. A methanol generation rate of 372.1 μmol h^{-1} g_{cat}^{-1}, and 100% RhB removing efficiency within 1 h were achieved by using 5wt% WS_2/g-C_3N_4 heterojunction, which were improved greatly compared with pure g-C_3N_4. Based on detailed investigations of the photochemical properties, the heterojunction structure of WS_2/g-C_3N_4 composite was correlated with their electron-transfer efficacy and the overall reaction efficiency. The results show that the band structure coordination between WS_2 and g-C_3N_4 made it possible to construct a structure of heterojunction. The photo-induced electrons in the CB of g-C_3N_4 would transfer to the CB of WS_2 before recombination with holes in VB of g-C_3N_4, so that the recombination of electron–hole pairs was eliminated and coefficient of utilization of photo-induced electrons was improved greatly. This work provides a novel platform for the efficient and sustained production of a broad range of chemicals and fuels from sunlight.

Conflicts of interest

The authors declare no conflicts of interest.

Acknowledgements

Notes and references

1 S. Ye, R. Wang, M.-Z. Wu and Y.-P. Yuan, *Appl. Surf. Sci.*, 2015, **358**, 15–27.
2 K. Sekizawa, K. Maeda, K. Domen, K. Koike and O. Ishitani, *J. Am. Chem. Soc.*, 2013, **135**, 4596–4599.
3 W. Wang, S. Wang, X. Ma and J. Gong, *Chem. Soc. Rev.*, 2011, **40**, 3703–3727.
4 Y. He, Y. Wang, L. Zhang, B. Teng and M. Fan, *Appl. Catal., B*, 2015, **168**, 1–8.
5 Y. Amao, *ChemCatChem*, 2011, **3**, 458–474.
6 F. S. Baskaya, X. Zhao, M. C. Flickinger and P. Wang, *Appl. Biochem. Biotechnol.*, 2010, **162**, 391–398.
7 B. C. D. Obert and R. Obert, *J. Am. Chem. Soc.*, 1999, **121**, 12192–12193.
8 X. Tong, B. El-Zahab, X. Zhao, Y. Liu and P. Wang, *Biotechnol. Bioeng.*, 2011, **108**, 465–469.
9 H. Wu, C. Tian, X. Song, C. Liu, D. Yang and Z. Jiang, *Green Chem.*, 2013, **15**, 1773–1789.
10 Y. Jiang, Q. Sun, L. Zhang and Z. Jiang, *J. Mater. Chem.*, 2009, **19**, 9068–9074.
11 X. Ji, Z. Su, P. Wang, G. Ma and S. Zhang, *Small*, 2016, **12**, 4753–4762.
12 X. Ji, Z. Su, P. Wang, G. Ma and S. Zhang, *ACS Nano*, 2015, **9**, 4600–4610.
13 F. L. Yang, F. F. Xia, J. Hu, C. Z. Zheng, J. H. Sun and H. B. Yi, *RSC Adv.*, 2018, **8**, 1899–1904.
14 K. Xu and J. Feng, *RSC Adv.*, 2017, **7**, 45369–45376.
15 P. Wang, I. Sinev, F. Sun, H. Li, D. Wang, Q. Li, X. Wang, R. Marschall and M. Wark, *RSC Adv.*, 2017, **7**, 42774–42782.
16 X. Wang, K. Maeda, A. Thomas, K. Takanabe, G. Xin, J. M. Carlsson, K. Domen and M. Antonietti, *Nat. Mater.*, 2009, **8**, 76–80.
17 P. Niu, L. Zhang, G. Liu and H.-M. Cheng, *Adv. Funct. Mater.*, 2012, **22**, 4763–4770.
18 J. Liu and M. Antonietti, *Energy Environ. Sci.*, 2013, **6**, 1486–1493.
19 Z. Tong, D. Yang, Z. Li, Y. Nan, F. Ding, Y. Shen and Z. Jiang, *ACS Nano*, 2017, **11**, 1103–1112.
20 Z. Tong, D. Yang, Y. Sun, Y. Nan and Z. Jiang, *Small*, 2016, **12**, 4093–4101.
21 G. Liu, P. Niu, C. H. Sun, S. C. Smith, Z. G. Chen, G. Q. Lu and H. M. Cheng, *J. Am. Chem. Soc.*, 2010, **132**, 11642–11648.
22 X. C. Wang, X. F. Chen, A. Thomas, X. Z. Fu and M. Antonietti, *Adv. Mater.*, 2009, **21**, 1609–1612.
23 X. Lu, Q. Wang and D. Cui, *J. Mater. Sci. Technol.*, 2010, **26**, 925–930.
24 Y. He, L. Zhang, M. Fan, X. Wang, M. L. Walbridge, Q. Nong, Y. Wu and L. Zhao, *Sol. Energy Mater. Sol. Cells*, 2015, **137**, 175–184.
25 Y. Liu, X. She, X. Zhang, C. Liang, J. Wu, P. Yu, Y. Nakanishi, B. Xie, H. Xu, P. M. Ajayan and W. Yang, *RSC Adv.*, 2017, **7**, 55269–55275.
26 B. Peng, P. K. Ang and K. P. Loh, *Nano Today*, 2015, **10**, 128–137.

27 Q. Lu, Y. Yu, Q. Ma, B. Chen and H. Zhang, *Adv. Mater.*, 2016, **28**, 1917–1933.

28 B. Mahler, V. Hoepfner, K. Liao and G. A. Ozin, *J. Am. Chem. Soc.*, 2014, **136**, 14121–14127.

29 Y. Hou, Y. Zhu, Y. Xu and X. Wang, *Appl. Catal., B*, 2014, **156–157**, 122–127.

30 M. S. Akple, J. Low, S. Wageh, A. A. Al-Ghamdi, J. Yu and J. Zhang, *Appl. Surf. Sci.*, 2015, **358**, 196–203.

31 Y. Ma, J. Li, E. Liu, J. Wan, X. Hu and J. Fan, *Appl. Catal., B*, 2017, **219**, 467–478.

32 X. Xu, Y. Liu, Y. Zhu, X. Fan, Y. Li, F. Zhang, G. Zhang and W. Peng, *ChemElectroChem*, 2017, **4**, 1498–1502.

33 T. Zhou, Y. Xu, H. Xu, H. Wang, Z. Da, S. Huang, H. Ji and H. Li, *Ceram. Int.*, 2014, **40**, 9293–9301.

34 G. Pagona, C. Bittencourt, R. Arenal and N. Tagmatarchis, *Chem. Commun.*, 2015, **51**, 12950–12953.

35 A. Akhundi and A. Habibi-Yangjeh, *Ceram. Int.*, 2015, **41**, 5634–5643.

36 J. Lei, Y. Chen, F. Shen, L. Wang, Y. Liu and J. Zhang, *J. Alloys Compd.*, 2015, **631**, 328–334.

37 H. Xiao, W. Wang, G. Liu, Z. Chen, K. Lv and J. Zhu, *Appl. Surf. Sci.*, 2015, **358**, 313–318.

38 Y. He, J. Cai, T. Li, Y. Wu, Y. Yi, M. Luo and L. Zhao, *Ind. Eng. Chem. Res.*, 2012, **51**, 14729–14737.

39 T. Li, L. Zhao, Y. He, J. Cai, M. Luo and J. Lin, *Appl. Catal., B*, 2013, **129**, 255–263.

40 X. Wang, K. Maeda, A. Thomas, K. Takanabe, G. Xin, J. M. Carlsson, K. Domen and M. Antonietti, *Nat. Mater.*, 2009, **8**, 76–80.

41 X. Wang, X. Chen, A. Thomas, X. Fu and M. Antonietti, *Adv. Mater.*, 2009, **21**, 1609–1612.

42 Y. Wang, J. S. Zhang, X. C. Wang, M. Antonietti and H. R. Li, *Angew. Chem., Int. Ed.*, 2010, **49**, 3356–3359.

43 D. Portehault, C. Giordano, C. Gervais, I. Senkovska, S. Kaskel, C. Sanchez and M. Antonietti, *Adv. Funct. Mater.*, 2010, **20**, 1827–1833.

44 L. Lin, H. Ou, Y. Zhang and X. Wang, *ACS Catal.*, 2016, **6**, 3921–3931.

45 S. Thaweesak, S. Wang, M. Lyu, M. Xiao, P. Peerakiatkhajohn and L. Wang, *Dalton Trans.*, 2017, **46**, 10714–10720.

46 S. Zhang, L. Gao, D. Fan, X. Lv, Y. Li and Z. Yan, *Chem. Phys. Lett.*, 2017, **672**, 26–30.

47 Z. A. Lan, Y. Fang, Y. Zhang and X. Wang, *Angew. Chem., Int. Ed.*, 2018, **57**, 470–474.

48 H. Ou, L. Lin, Y. Zheng, P. Yang, Y. Fang and X. Wang, *Adv. Mater.*, 2017, **29**, 1700008.

49 H. Ou, P. Yang, L. Lin, M. Anpo and X. Wang, *Angew. Chem., Int. Ed.*, 2017, **56**, 10905–10910.

50 S. Kang, Y. Fang, Y. Huang, L.-F. Cui, Y. Wang, H. Qin, Y. Zhang, X. Li and Y. Wang, *Appl. Catal., B*, 2015, **168**, 472–482.

51 Y. Hou, Z. Wen, S. Cui, X. Guo and J. Chen, *Adv. Mater.*, 2013, **25**, 6291–6297.

52 H. Katsumata, Y. Tachi, T. Suzuki and S. Kaneco, *RSC Adv.*, 2014, **4**, 21405–21409.

53 D. Voiry, H. Yamaguchi, J. Li, R. Silva, D. C. Alves, T. Fujita, M. Chen, T. Asefa, V. B. Shenoy, G. Eda and M. Chhowalla, *Nat. Mater.*, 2013, **12**, 850–855.

54 Z. Zhang, J. Huang, M. Zhang, Q. Yuan and B. Dong, *Appl. Catal., B*, 2015, **163**, 298–305.

55 S. C. Yan, Z. S. Li and Z. G. Zou, *Langmuir*, 2010, **26**, 3894–3901.

56 Y. Imanaka, T. Anazawa, T. Manabe, H. Amada, S. Ido, F. Kumasaka, N. Awaji, G. Sanchez-Santolino, R. Ishikawa and Y. Ikuhara, *Sci. Rep.*, 2016, **6**, 35593.

57 L. Ma, H. Fan, J. Wang, Y. Zhao, H. Tian and G. Dong, *Appl. Catal., B*, 2016, **190**, 93–102.

58 S. Kumar, T. Surendar, B. Kumar, A. Baruah and V. Shanker, *RSC Adv.*, 2014, **4**, 8132–8137.

59 W. Li, C. Feng, S. Dai, J. Yue, F. Hua and H. Hou, *Appl. Catal., B*, 2015, **168–169**, 465–471.

60 S. G. Kumar and K. S. R. K. Rao, *RSC Adv.*, 2015, **5**, 3306–3351.